

Article

Revealing High-Temperature Oxidation and Tensile Behaviors along with Underlying Mechanisms of a Titanium Alloy with Precipitated Titanium Silicide

Jinwen Lu ^{1,2,*}, Kaile Ji ³, Longchao Zhuo ^{3,*} , Bingqing Chen ^{4,*}, Hui Shao ³, Wangtu Huo ² and Yongqing Zhao ²¹ Xi'an Rarealloys Co., Ltd., Xi'an 710016, China² Advanced Materials Research Central, Northwest Institute for Nonferrous Metal Research, Xi'an 710016, China³ School of Materials Science and Engineering, Xi'an University of Technology, Xi'an 710048, China⁴ 3D Printing Research and Engineering Technology Center, AECC Beijing Institute of Aeronautical Materials, Beijing 100095, China

* Correspondence: lujwen@163.com (J.L.); zhuolongchao@xaut.edu.cn (L.Z.); hwtkjcb1984@163.com (B.C.); Tel./Fax: +86-29-82312156 (L.Z.)

Abstract: Titanium alloys, with their impressive strength relative to their weight, resistance to corrosion, and compatibility with biological systems, have found extensive applications in various industries. In high-temperature environments, especially within the aerospace sector, it is essential to advance titanium alloys that boast enhanced resistance to oxidation and superior mechanical characteristics. This work investigates the oxidation characteristics and mechanical performances at high temperatures of a titanium alloy with titanium silicide particles. Oxidation at temperatures of 600–700 °C over a span of 8–32 h led to the formation of protective oxide layers and moderate oxidation rates. However, accelerated oxidation and oxide spallation occurred after exposed at 800 °C for a period of 16 h, indicating inadequate oxidation resistance over 800 °C. Subsequent tensile tests at 650 °C revealed intricate dislocation patterns in the α -Ti matrix and their strong interaction with interfaces of α -Ti/Ti₅Si₃, which is indicative of an efficient load transfer between the precipitates and the matrix. Overall, this study offers fresh perspectives on the oxidation kinetics and the deformation processes of titanium alloys with in-situ Ti₅Si₃ particles at high temperatures. These insights will guide subsequent alloy development endeavors aiming to broaden the use of titanium alloys in increasingly challenging high-temperature settings.

Keywords: titanium alloys; in-situ; oxidation kinetics; high temperature tensile; microstructure

Citation: Lu, J.; Ji, K.; Zhuo, L.; Chen, B.; Shao, H.; Huo, W.; Zhao, Y.

Revealing High-Temperature Oxidation and Tensile Behaviors along with Underlying Mechanisms of a Titanium Alloy with Precipitated Titanium Silicide. *Coatings* **2023**, *13*, 2020. <https://doi.org/10.3390/coatings13122020>

Academic Editor: Maria Vittoria Diamanti

Received: 8 November 2023

Revised: 24 November 2023

Accepted: 28 November 2023

Published: 29 November 2023



Copyright: © 2023 by the authors. Licensee MDPI, Basel, Switzerland. This article is an open access article distributed under the terms and conditions of the Creative Commons Attribution (CC BY) license (<https://creativecommons.org/licenses/by/4.0/>).

1. Introduction

Due to their standout features, like their lightweight nature, superior strength, impressive corrosion resistance, biocompatibility, and absence of magnetic properties, titanium alloys have become indispensable in diverse industries [1]. These attributes have rendered titanium alloys indispensable in critical sectors, such as in aerospace, military, marine, automotive, and industrial applications [2]. In particular, the unique demands of titanium alloy applications under high-temperature conditions have prompted the need for innovations in the design of materials. Notably, the aerospace domain necessitates materials capable of enduring elevated temperatures and sustained stresses, making titanium alloys with an enhanced high-temperature performance vital for next-generation aero-engines and aircraft [3,4]. Consequently, efforts to enhance their high-temperature oxidation resistance and mechanical properties have become a focus of extensive research.

However, a challenge arises when titanium alloys encounter oxygen environments exceeding 600 °C; there is a risk of forming unstable oxides, with a subsequent detachment from the surface [5]. To address this issue, extensive research has been dedicated to

introducing ceramic particles with improved high-temperature durability, high modulus, and oxidation resistance [6–8]. It was found that TiB whiskers diminished the oxidation resistance in the titanium alloy, while Ti_5Si_3 particles bolstered the oxidation resistance by refining TiO_2 particles, thereby enhancing the toughness and compactness of the oxide layer [9]. The addition of LaB_6 significantly decreased the oxidation rate of titanium alloys at 600 °C [10]. The parabolic rate constants of the Ti-Al-Sn-Zr alloy at 750 °C and 850 °C decreased with the increase in the added SiC particles [11]. On the other hand, various titanium alloys incorporated with ceramic particles, such as TiC, TiB, NbC, Ti_3AlC , and La_2O_3 , have been shown to bolster their mechanical characteristics, particularly by elevating their flow stress [12–16]. Moreover, high strength–ductility synergy is highly required for titanium alloys with ceramic particles, both at room temperature and at elevated temperatures. This balance is vital to cut down production expenses and mitigate the potential for failures during usage.

During high-temperature deformation processes in particular, the grain boundary slip mechanism takes precedence. The grain boundaries are susceptible to microcrack formation due to the significantly reduced strength at elevated temperatures, and its rupture could lead directly to the onset and spread of microcracks [17,18]. Consequently, in comparison with the alloys reinforced with foreign particles from outside, titanium alloys with strengthening ceramic particles through in-situ precipitation have the advantages of fine reinforcements, clean reinforcement/matrix interfaces with no contamination, superior wettability and interfacial bonding, as well as low preparation cost [19]. In addition, silicide ceramics demonstrated better deformation characteristics than other compounds like carbides and borides [20]. Specifically, the silicide of Ti_5Si_3 exhibits a high melting point, low density, pronounced creep resistance, high fracture toughness over 1000 °C, good oxidation resistant behavior, and a thermal expansion coefficient closely matching that of titanium [21–23]. In this context, this work presents the investigation of a titanium alloy incorporating titanium silicide precipitates. Given the material's potential, this study focuses on understanding its oxidation behavior and mechanical response at high temperatures. By systematically exploring the interplay of in-situ Ti_5Si_3 precipitates and the alloy matrix, this investigation contributes to advancing the comprehension of high-temperature alloy behavior and paves the way for novel applications in aerospace and other demanding environments.

2. Materials and Methods

In this research, we investigated a high-strength titanium alloy with the following composition: Ti-4.5Al-2.5Si-2Mo-2Zr-2Nb-1Sn-1Ta-1W-1Hf (wt.%). The initial step involved melting the respective raw elemental materials 3–4 times in a vacuum arc furnace. Subsequently, the billet underwent hot forging at 1050 °C, followed by hot rolling at 850 °C. To analyze the phase composition, the X-ray diffraction (XRD) analysis was conducted on a 1 cm × 1 cm × 1 cm sample using a 7000S X-ray diffractometer (XRD, Shimadzu, Kyoto, Japan), employing Cu $K\alpha$ radiation (wavelength $\lambda = 1.5418 \text{ \AA}$) at an operational setting of 30 kV and 30 mA. The scans covered a 2θ range, extending from 20° to 80°, utilizing a step size of 0.02°. The scanning proceeded at a speed of 1° per minute. To enhance the diffraction intensity, the sample was set to rotate at a rate of 30 revolutions per minute. An FEI G20 Transmission Electron Microscope (TEM, Thermo Fisher Scientific, Waltham, MA, USA) further validated the microstructure. For transmission electron microscopy (TEM) sample preparation, electrochemical thinning was employed. This method, also known as electropolishing, provides several advantages over traditional ion thinning techniques, particularly for materials like titanium alloys that can be challenging to prepare due to their unique chemical and physical properties. Electrochemical thinning offers a gentler approach that minimizes heat and stress effects on the sample, allows precise control over the thickness, and often enables faster preparation. This was meticulously carried out using an 8% perchloric acid solution in ethanol. The procedure was executed at a controlled voltage of 50 V, with the temperature meticulously maintained at 35 °C, ensuring optimal

conditions for sample preparation. In addition, titanium alloy plates were fashioned into 8 mm × 8 mm × 8 mm squares using wire electric discharge. These specimens were then ground, cleaned, and prepped for oxidation tests. Oxidation tests were conducted in a tubular furnace, with static air as the controlled environment. Specimens were put into the furnace and exposed to temperatures of 600 °C, 700 °C, and 800 °C. Following specific durations (8 h, 16 h, 24 h, and 32 h), they were allowed to cool by air until room temperature. An electronic balance, accurate to 0.0001 g, recorded the sample mass change. The below formula was employed to compute the oxidative mass gain for each sample pre- and post-oxidation:

$$\Delta w = \frac{\Delta m}{S} \quad (1)$$

Here, Δw delineates the weight increase due to oxidative per unit surface area, quantified as mg/cm². The term Δm signifies the differential mass of the specimens pre- and post-oxidation, expressed in mg; S demarcates the aggregate surface area of the given specimen, measured in cm². Subsequently, the oxidation progression was visualized by mapping the kinetic curves between Δw and the time of t . In alignment with Wagner's oxidation paradigm, the weight augmentation Δw is concomitant with the duration of oxidation t , as expounded in reference [24].

$$(\Delta w)^n = k_p t \quad (2)$$

where Δw signifies the increase in mass from oxidation per unit of surface area; n denotes the index of the reaction; k_p stands for the constant of the reaction rate; and t designates the time period of oxidation. Additionally, the reliance of the temperature on k_p can be calculated according to the well-known Arrhenius formula [25].

The samples' overall appearances and element distribution after undergoing oxidation were examined using a JEOL-6700 scanning electron microscope (SEM, JEOL, Tokyo, Japan), supplemented with the energy dispersive X-ray spectroscopy (EDX). Before SEM analysis, the samples were grinded and polished with the following etch in a chemical mixture (HF: HNO₃: H₂O at a ratio of 1:2:5 by volume) for a duration of 10–15 s. Subsequently, they were ultrasonically cleaned in both alcohol and water. After preheating for 5 min at a specified temperature, the tensile properties were evaluated at a steady strain rate of $5 \times 10^{-4} \text{ s}^{-1}$ using an Instron-3382 at elevated temperatures of 550 °C, 600 °C, and 650 °C.

3. Results and Discussions

Figure 1a displays the XRD profiles of the titanium alloy, characterized by the presence of the α phase, β phase, and a minor quantity of the Ti₅Si₃ phase. A more in-depth view into the microstructural details can be seen in Figure 1b–o, which includes bright-field, STEM elemental distribution illustrations using EDX and SAED data. Figure 1m–o, obtained from the three blue regions indicated in Figure 1b, has been precisely indexed as α -Ti, β -Ti, and Ti₅Si₃, respectively, providing clear evidence of the crystalline structures present in the sample. More specifically, hexagonal structured Ti₅Si₃ was indexed according to both the interplanar spacing and angle verification to be the 2D projection from the zone axis of [10-1]. The interplanar spacings of the 010, 111, and 101 planes of this phase, as measured by the inverse of the lengths of the three sides from the respective spot to the transmission spot, match well with the standard values, with a tolerance of only 0.07 Å. Meanwhile, the tolerance in angles is found to be 1° only upon angle verification. The comparative reduction in Ti and the increase in Si made the morphology of the Ti₅Si₃ particles evident, as discerned in Figure 1d,f. Additionally, Figure 1c shows partial Hf dissolution into Ti₅Si₃, corroborated by an EDX quantitative analysis result of Ti_{66.47}Si_{24.51}Al_{0.51}Zr_{0.57}Mo_{0.73}Hf_{4.33}Ta_{2.05}W_{0.83} in weight percentage. The unobvious concentration of Ta, W, and Mo (Figure 1k,l,g) in the spherical Ti₅Si₃ was attributed to their higher segregation in β -Ti; however, it is certain that the incorporation of Hf, Ta, W, and Mo would affect the properties of the silicide by altering its stability, diffusion kinetics, electron structure, and other performance factors. Previous research has indicated that the introduction of Hf enhanced the nucleation of fine Ti₅Si₃

particles, reducing the overall brittleness by leveraging its lower solution enthalpy in Ti_5Si_3 compared to both α -Ti and β -Ti [26,27]. STEM elemental distribution also revealed that particles A and B have much lower Si content compared to particle C, indicating that they are Ti-rich phases rather than silicides. As illustrated in Figure 1i,k,l, the images revealed an area enriched with β -Ti stabilizing elements, including Nb, Ta, and W, representing the β -Ti phase. In contrast, the surrounding area could be identified as the α -Ti phase.

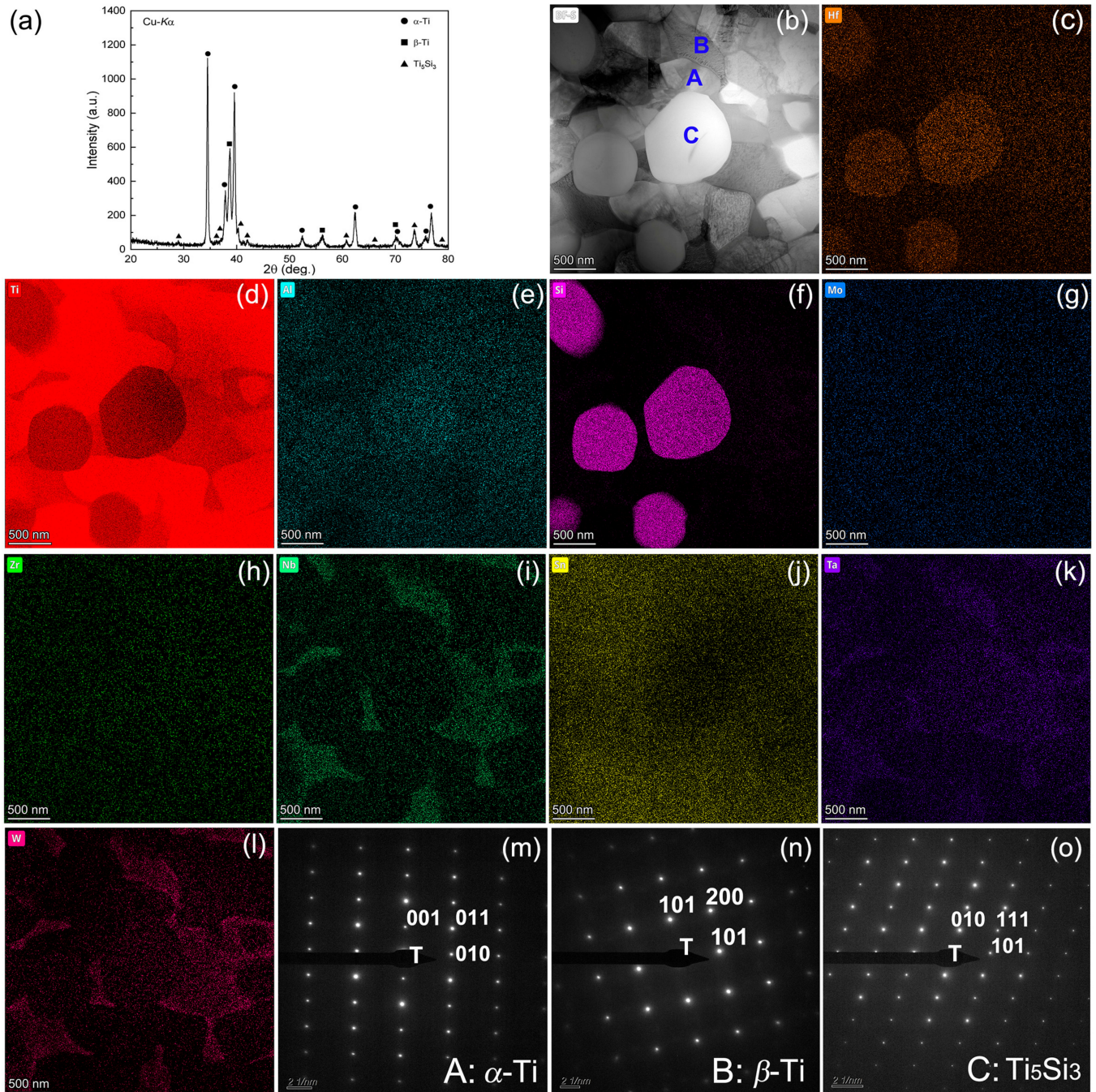


Figure 1. XRD pattern of the titanium alloy (a), bright field TEM image (b), elemental distribution maps (c–l), SAED patterns (m–o) taken from regions A, B and C in (b).

For potential high temperature applications, understanding the oxidation behavior of the titanium alloy is crucial. The alloy samples underwent oxidation in open air at temperatures of 600 °C, 700 °C, or 800 °C for 8–32 h. The resulting mass change per unit

area after oxidation is displayed in Figure 2a. It is evident that the rate of oxidation exhibited a gradual increase from 600 °C to 800 °C, with oxidation being slow at 600 °C and 700 °C, and rapid at 800 °C. In accordance with metal oxidation kinetics, the initial small weight increase at 800 °C for 8 h suggests the formation of a protective oxide film. However, as the duration of exposure increased, non-protective oxidation films accelerated the oxidation rate. By logging both sides of Equation (2) and graphing the variation of $\ln(\Delta m)$ against $\ln t$, a linear trend emerged, as shown in Figure 2b. This allows for the extraction of the reaction index n and the rate constant k_p using linear regression. The obtained values were approximately 1.97 at 600 °C, 2.32 at 700 °C, and 1.69 at 800 °C for n , as well as 0.00714, 0.0775, and 0.4813 for k_p , respectively. The oxidation mechanism is predominantly controlled by diffusion processes. When $n = 1$, the oxidation reaction rate follows a linear law, governed by the oxidation reaction rate of oxygen and matrix metal [28]. For $n = 2$, the oxidation reaction rate follows a parabolic law, driven by reactant diffusion in the oxide film [29]. When n takes a value between 1 and 2, the oxidation process involves both reactant diffusion in the oxide film and oxidation reaction between oxygen and the base metal [30]. The parabolic rate constant k_p signifies the alloy oxidation rate. Figure 2 illustrates that n is 1.97 at 600 °C with a small k_p value, indicating excellent oxidation resistance. At 700 °C, the n value of 2.32 indicated a diffusion-controlled oxidation mechanism with effective substrate protection via the oxide film [31]. At 800 °C, an n value of smaller than 2 implies interface reaction control between oxygen and the oxide film/substrate, and a relatively large k_p value suggests that the oxidation process was potentially influenced by stress, pores, and grain boundaries [32]. As the oxidation temperature increased, the values of n decreased with the increasing k_p , reflecting combined diffusion and surface oxidation reaction control. Linear analysis, shown in Figure 2c, provided an oxidation activation energy value of 164.1 kJ/mol, which shed light on the oxide growth process and the diffusion of oxygen into the matrix [33].

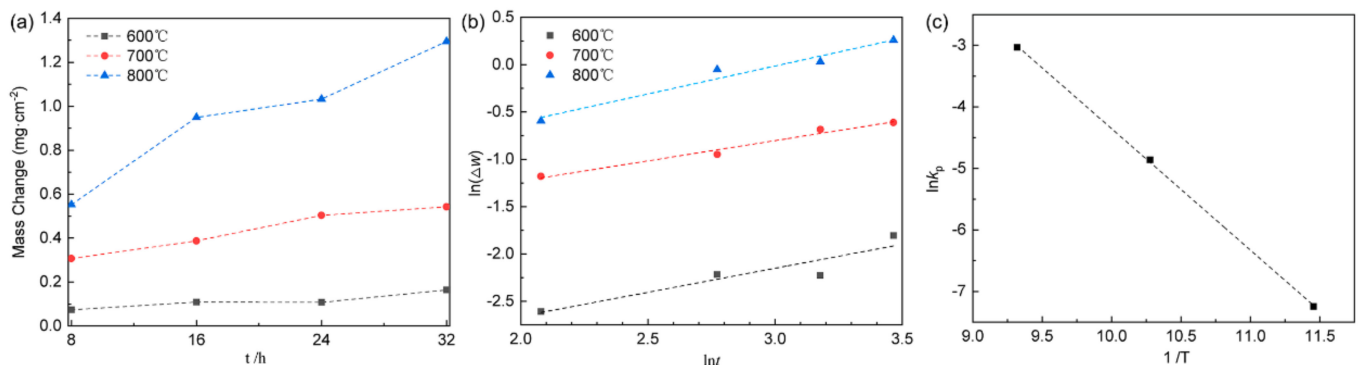


Figure 2. Oxidation kinetics of Δw versus t (a), the plot of $\ln(\Delta w)$ against $\ln(t)$ (b), and the graph of $\ln k_p$ against $1/T$ (c) for the alloy subjected to oxidation at temperatures of 600 °C, 700 °C and 800 °C.

Figure 3 depicts the overall color presentation of the alloy after oxidation at temperatures ranging between 600 and 800 °C for various time durations. It can be seen that, at 600 °C, the surface color of the alloy shifted from light-yellow to light-brown, eventually progressing to dark-yellow and culminating in a blue hue as oxidation proceeded. Similarly, oxidation at 700 °C resulted in color transitions from yellowish-brown to blue, while oxidation at 800 °C induced a change from blue to a gradually light-green shade. The intricate surface color variations of oxidized titanium alloys arise from factors including the oxide layer composition, layer compactness, thickness, interference effects of light, surface roughness, luminous flux of the oxide film, refractive index, and reflectance [34–36]. As the titanium alloys underwent surface oxidation, a diverse range of titanium oxides formed, each contributing distinct colors. Therefore, the uneven coloration of the oxide film can be attributed to the formation and content of these oxides. The porous oxide layer's capacity to absorb light affected the interplay between light bouncing off the oxide film's

surface and the light reflecting at the oxide/titanium boundary. This leads to intricate visible hues characterized by varying wavelengths and proportions. It is worth noting that TiO_2 with crystalline irregularities can display a spectrum of colors like yellow, blue, and white [37,38].

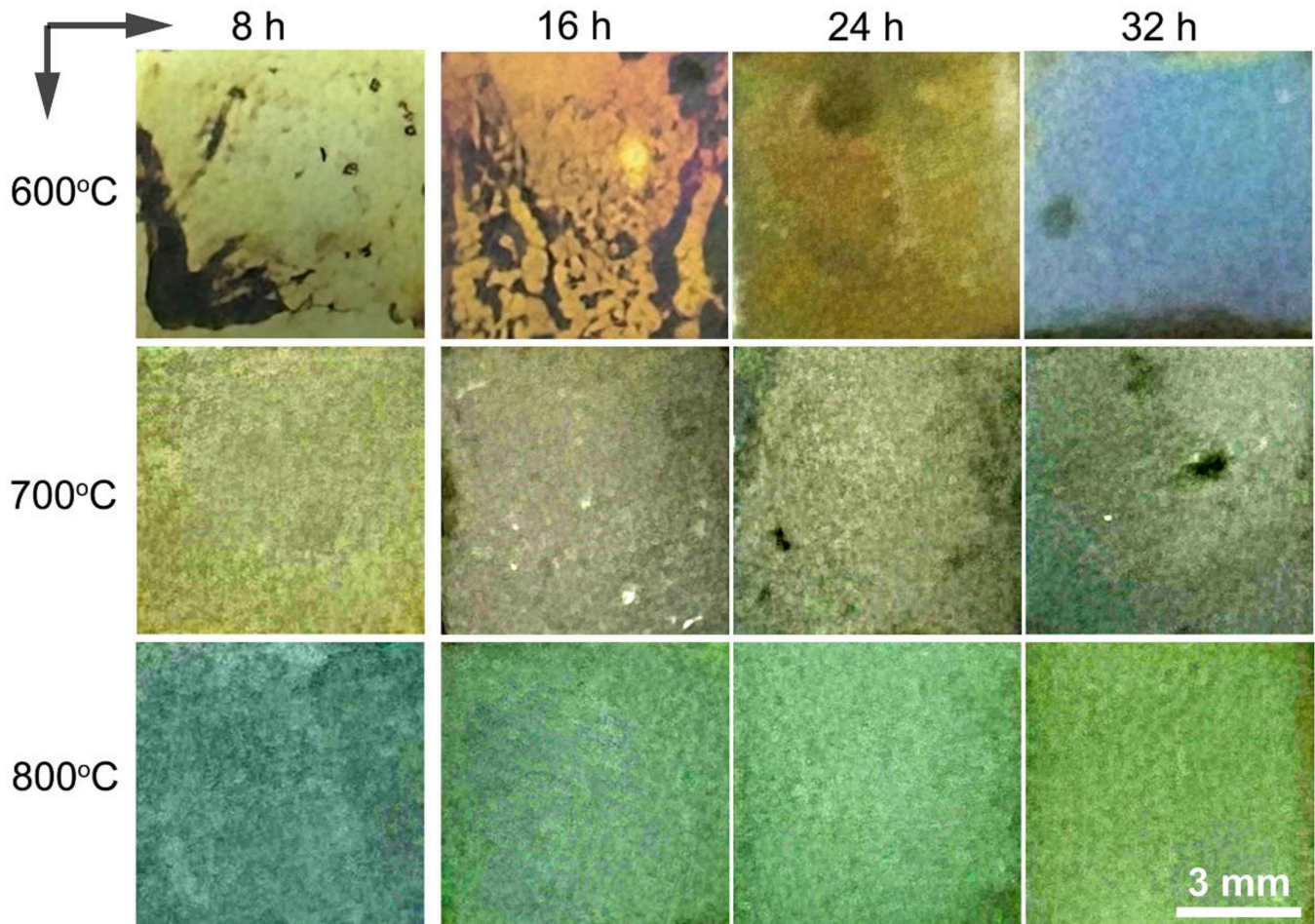


Figure 3. Surface view of the alloy after oxidation at 600–800 °C for 8 h, 16 h, 24 h, and 32 h.

Figure 4 displays the XRD patterns from the oxide layers that developed on the alloy surface after exposure to various temperatures and durations. When subjected to oxidation at 600 °C, a notable intensity in the Ti diffraction peak was observed. However, as the oxidation duration extended, there was a corresponding increase in the intensity of the TiO_2 peaks, accompanied by a gradual reduction in the Ti peak intensity. Conversely, at 800 °C, a significant decline in the Ti peak intensity was observed, coinciding with an elevation in the TiO_2 intensity. This trend signifies a marked decrease in the alloy's resistance to oxidation. The observed variations in the oxide layer composition and content under distinct oxidation conditions align with the discernible differences in the oxide layer colors, as depicted in Figure 3. Importantly, the prevalence of TiO_2 on the alloy surface becomes evident in cases of oxidation at 800 °C.

Figure 5 depicts the surface view of the alloy after oxidation at temperatures between 600 °C and 800 °C for durations of 8 h, 16 h, 24 h, and 36 h, respectively. The oxide film formed on the surface was relatively dense and exhibited bright white characteristics (Figure 5a–d) at 600 °C, attributable to the lower oxidation temperature and partial preferential oxidation behavior occurring along the phase boundaries with high energy and diffusion rates. The oxidation reaction rate primarily governed the process at 600 °C. With the increase to the higher temperature of 700 °C (Figure 5e–h), a generally flat surface was

observed, while the emergence of small holes was notable with the increasing oxidation time. This phenomenon might be attributed to the incomplete oxidation of positions occupied by oxidation-resistant Ti_5Si_3 particles during the process. These particles acted as barriers against further oxygen ingress, leading to the formation of small surface pores. The oxidation kinetics curve, which depicts a deceleration in the oxidation rate as the oxidation time increases, supports the above observation. The thicker oxide layer arising from the greater diffusion distance of the titanium ions curtailed the surface oxidation reaction rate, enabling a protective role. In contrast, oxidation at $800\text{ }^\circ\text{C}$ yielded an uneven surface with nodules (Figure 5i–l). After 8 h of oxidation, a few pores persisted due to the high oxidation resistance of Ti_5Si_3 . However, extended holding times resulted in the peeling off of oxide layers from the surface due to residual stress differences between the oxide layer and substrate arising from their different thermal expansion coefficients. Following 32 h of oxidation, oxidized particles coarsened, engendering a chaotic and loose surface structure with short rods and irregular pores, facilitating oxygen diffusion. The heightened oxide detachment indicated compromised high-temperature oxidation resistance, in accordance with previous oxidation kinetics analysis. EDX analysis on the alloy oxidized for 32 h at $800\text{ }^\circ\text{C}$ corroborated the complete formation of TiO_2 on the surface. Therefore, Ti_5Si_3 demonstrates a dual role in the oxidation behavior and mechanisms of the alloy. It acted as a protective barrier at the lower temperatures of $600\text{ }^\circ\text{C}$ and $700\text{ }^\circ\text{C}$, retarding oxidation through selective oxide formation. However, at the higher temperature of $800\text{ }^\circ\text{C}$, the dissolution of Ti_5Si_3 accelerated the oxidation process by altering the alloy's microstructure and providing pathways for oxygen diffusion. In essence, the presence of Ti_5Si_3 particles in the alloy played a crucial role in its oxidation tendencies, shaping the emergence of protective oxide barriers and dictating the pace at which oxidations transpired. The nature of this influence varies at different temperatures, leading to distinctive mechanisms that are essential for comprehending the alloy's oxidation behavior at elevated temperatures. Comparatively, as Ti-6Al-4V contains a toxic element of vanadium, the activation energy for oxygen oxidation was only 126 kJ/mol [39]. In addition, a typical high-temperature titanium alloy of Ti-6Al-7Nb consists of Al_2O_3 , TiO, and TiO layers, in which the addition of 7 wt.%Nb and 1 wt.%W hindered the diffusion of oxygen, and the effect of Al on the oxygen absorption fostered the formation of a uniform and compact oxide film on the exterior [40]. Therefore, the present alloy showed relatively high oxidation resistance.

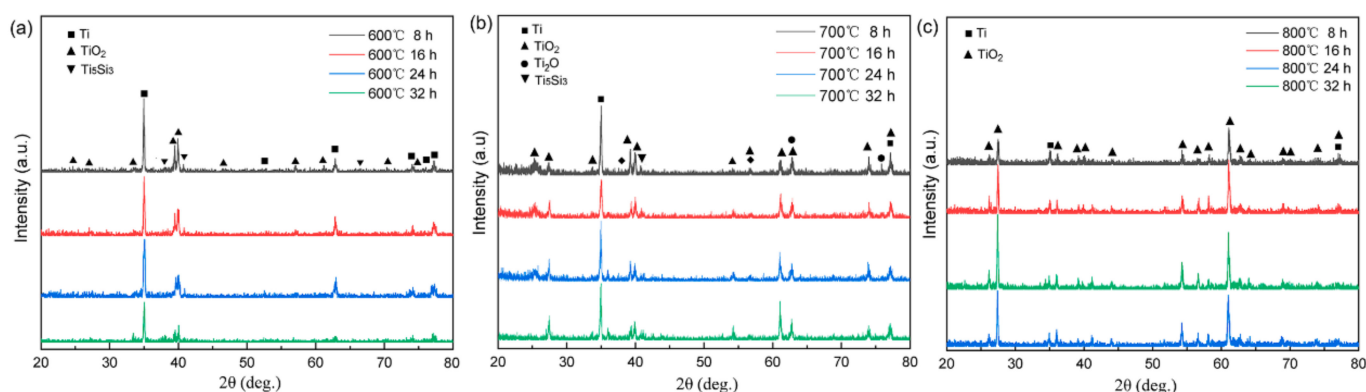


Figure 4. XRD patterns of the titanium alloy after oxidation at respective $600\text{ }^\circ\text{C}$ (a), $700\text{ }^\circ\text{C}$ (b) and $800\text{ }^\circ\text{C}$ (c) for 8 h, 16 h, 24 h, and 32 h.

Figure 5 presents a surface view of the titanium alloy subjected to oxidation at $600\text{--}800\text{ }^\circ\text{C}$ over 8 h, 16 h, 24 h, and 32 h (a–l), with spot analysis on the oxidated sample at $800\text{ }^\circ\text{C}$ for 32 h (m).

The specific requirements of certain titanium alloys for applications in high-temperature environments, coupled with the inevitability of oxidation reactions during processing without a protective atmosphere, necessitate an examination of their high-temperature

deformation behavior [41]. Here, we conducted tests and analyses to investigate the response of the alloy under atmospheric exposure. Figure 6a,b presents the engineering stress-strain data obtained from high-temperature tensile tests conducted at 550 °C, 600 °C, and 650 °C. At 550 °C, the tensile properties were characterized by a yield strength (σ_y) of 227.54 MPa, a tensile strength (σ_t) of 305.4 MPa, and a value of elongation (ϵ) of up to 107.7%. For the tests at 600 °C, the values were 113.52 MPa for σ_y , 142.58 MPa for σ_t , and 253.1% for ϵ . Similarly, at 650 °C, the tensile properties were 42.41 MPa for σ_y , 54.11 MPa for σ_t , and 694.7% for ϵ .

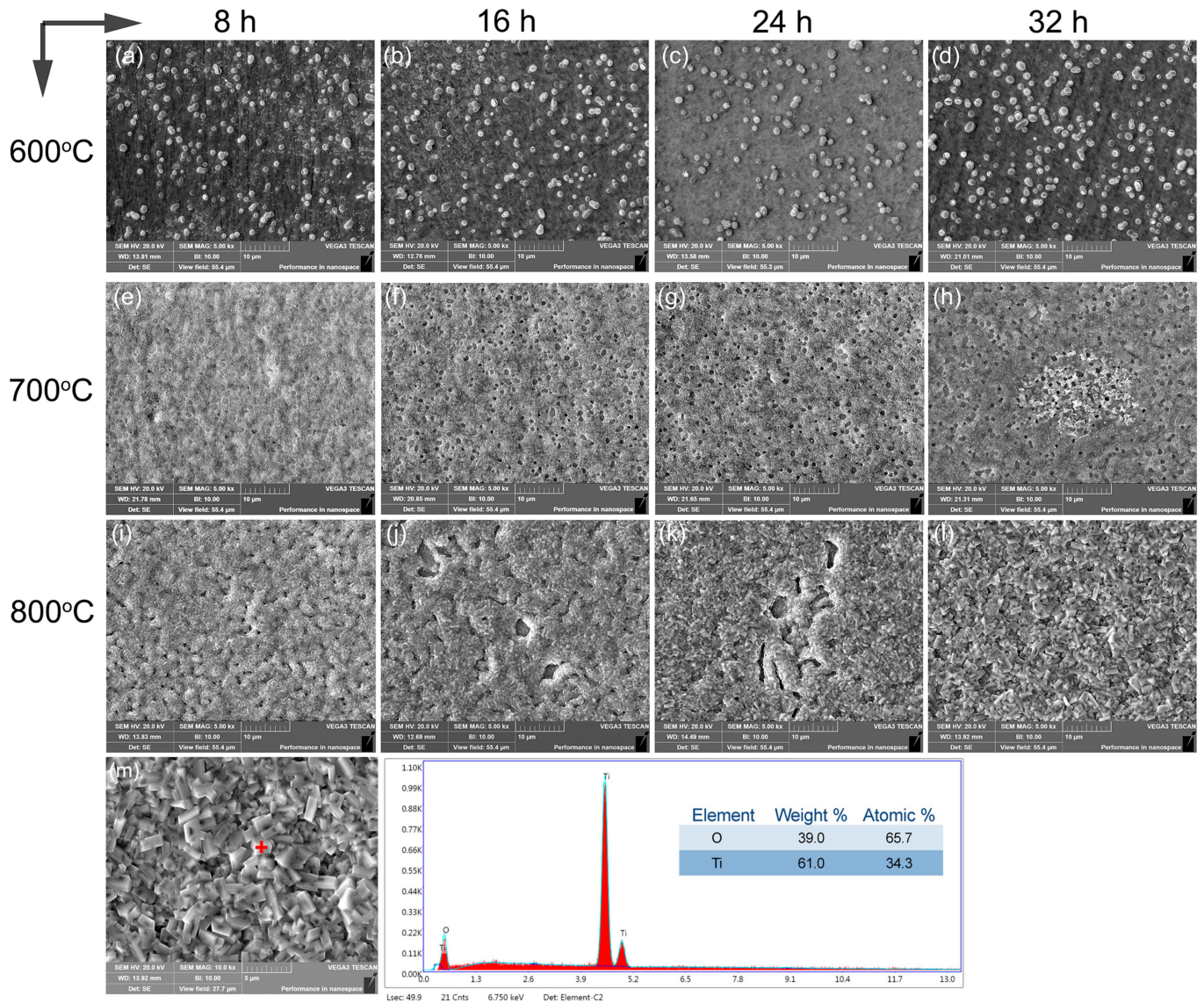


Figure 5. Surface view of the titanium alloy subjected to oxidation at 600–800 °C over 8 h, 16 h, 24 h, and 32 h (a–l), with a spot analysis on the oxidated sample at 800 °C for 32 h (m).

Figure 6c shows images of the alloy specimens used for the high-temperature tensile tests before and after failure at temperatures of 550 °C, 600 °C, and 650 °C. It is evident that the strength decreased as the deformation temperature increased, while its plasticity gradually increased. This occurrence can be considered to be a result of the diminished strength in both the grain and phase boundaries and the weakening of the solid solution strengthening effect [15,17]. During thermal deformation, the magnitude of flow stress hinges on the balance between dynamic softening and work hardening processes. Enhanced thermal activation at higher temperatures increases the frequency of atomic jump behavior and reduces

the energy required for dislocations to surmount barriers [42]. As a result, the critical shear stress decreased, leading to lower flow stress. Meanwhile, thermally activated dynamic recovery and recrystallization processes occurred, consuming dislocations and decreasing flow stress [43]. The fracture morphologies of the alloy specimens after high-temperature tensile deformation are presented in Figure 6d–f. The occurrence of slip between the adjacent β and α colonies was heavily influenced by their crystal orientation, rendering them susceptible to crack nucleation. In general, stress concentration, caused by uncoordinated deformation at phase boundaries between the α , β , and Ti_5Si_3 phases, triggered crack nucleation. The specimens showcase a myriad of evenly distributed and delicate dimples, enriched with an abundance of tear edges, indicative of substantial plastic deformation capacity. It is noteworthy that the stress concentration during high-temperature stretching is not uniformly distributed, owing to the different thermal expansion coefficients for the three constituting phases. Specifically, at 600 °C and 650 °C with high deformations (253.1% and 694.7%), internal cracks emerged in some large Ti_5Si_3 particles (~10 μm), while no interface debonding occurred. This observation underscores the robust interface bonding strength between in-situ Ti_5Si_3 and the surrounding matrix.

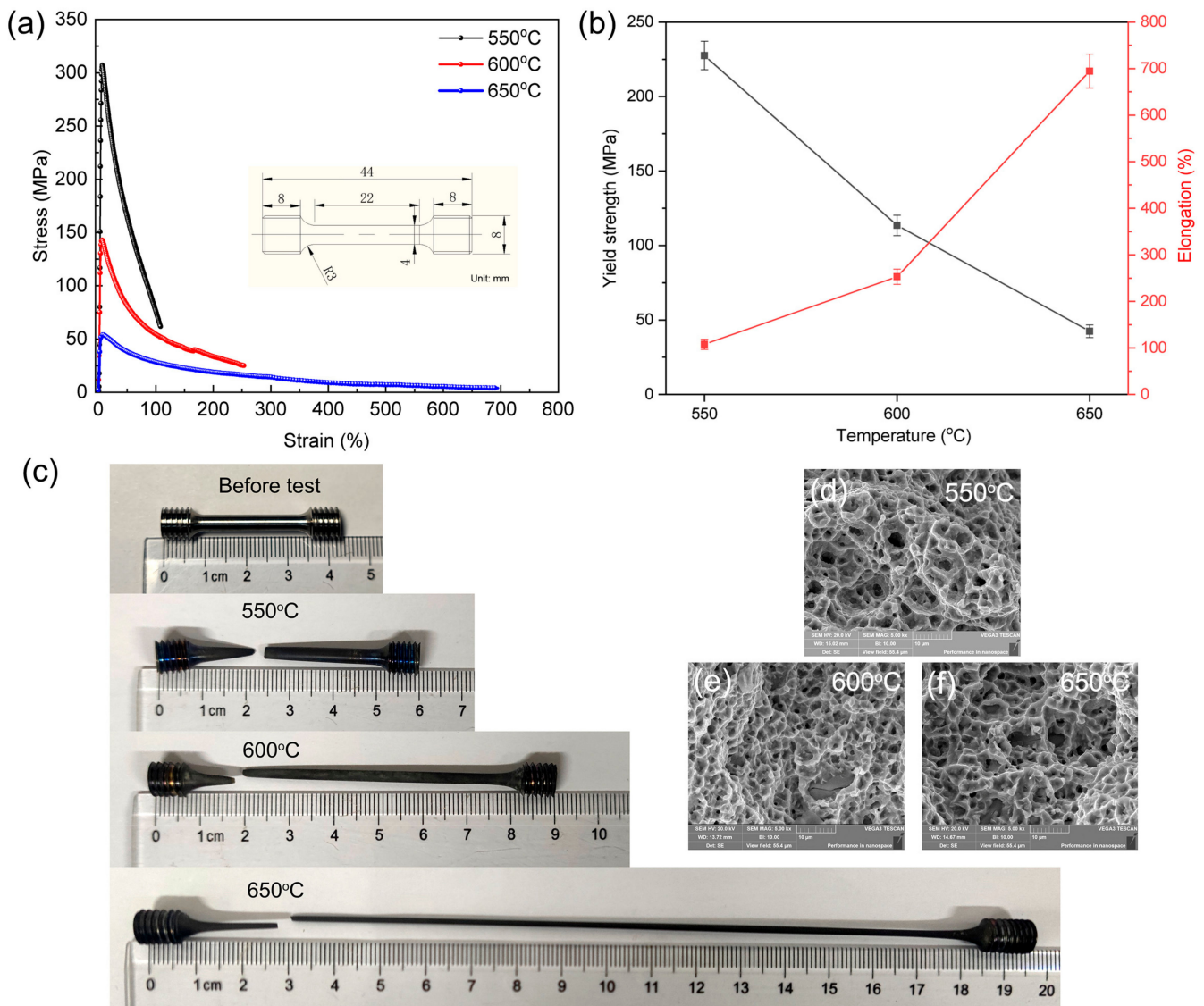


Figure 6. High temperature tensile stress-strain curves with the test sample size in the inset (a), summarized yield strength and elongation values with the change of test temperature (b), the real sample pictures before test and after failure (c), as well as fractography images (d–f).

The essence of high-temperature deformation for alloys is the interplay between dynamic hardening and softening mechanisms [17,44]. Dynamic hardening involves dislocation accumulation, the formation of locked dislocation configurations, and energy consumption for dislocation initiation. The dynamic softening mechanisms include dynamic recovery, dynamic recrystallization, and insulation heating [45]. Dynamic recovery facilitates the migration and reaction of dislocations, leading to reduced dislocation densities. Dynamic recrystallization involves the movement of recrystallized grain boundaries [46]. The plastic deformation of polycrystalline titanium alloys is predominantly governed by intragranular and grain boundary slips. The dynamics of α slip and the interplay between α/β phase slip existed within intragranular slip. Conversely, grain boundary movements incorporate both β grain boundary slip and α boundary slip [17]. The TEM analysis here sheds light on the resulting high strength–ductility synergy observed during high-temperature tensile deformation.

A complex dislocation structure was notably observed within the α -Ti phase post-deformation (Figure 7a,b). As the temperature increased, the critical resolved shear stress decreased sharply, leading to both pyramidal and basal slips during high-temperature deformation [47,48]. The reinforcing Ti_5Si_3 particles impeded excessive dislocation motion, resulting in dislocation tangles or pile-ups at the phase boundaries (Figure 7a,b). Elevated dynamic recovery occurred within the metastable β phase, and with the increased deformation temperature, both the intragranular and grain boundary strengths declined, albeit with a sharper reduction in the grain boundary strength. At 650 °C, the weakest region in the polycrystalline alloys was the grain boundary. Consequently, the mechanism of grain boundary slip took precedence during elevated temperature deformation, with the grain boundaries being prone to microcrack formation due to their inherent weakness [17]. For the phase boundaries between Ti_5Si_3 and the matrix, however, it can be observed that the in-situ precipitates displayed strong wettability and interfacial bonding.

A complex dislocation structure was notably observed within the α -Ti phase post-deformation (Figure 7a,b). The complex dislocation assemblies within the α -Ti phase (Figure 7a) indicated the occurrence of dynamic strain aging during hot deformation [47], which restricted dislocation motion through the diffusion of solute atoms to dislocation cores, enabling dislocation tangles and junctions [48]. The formed dislocation cell structures signified the dynamic balance between work hardening and softening [49]. As the temperature increased, the critical resolved shear stress decreased sharply, leading to extensive basal, pyramidal, and cross slips during high-temperature deformation [50,51]. The high stacking fault energy of α -Ti contributed to extensive cross slips near the peak strains [52]. The cross-slip intersection provides more deformation modes and facilitates dynamic recrystallization. Moreover, the dislocation pile-ups along the $\alpha/\text{Ti}_5\text{Si}_3$ phase boundaries (Figure 7b) produce a substantially increased stress concentration that could promote crack initiation. Nevertheless, the excellent interface strength withstood the stress concentration without incurring debonding. This is due to the sound metallurgical bonding and lattice coherency in the in-situ synthesized phases. The reinforcing Ti_5Si_3 particles impeded excessive dislocation motion, resulting in dislocation tangles or pile-ups at phase boundaries (Figure 7a,b). Elevated dynamic recovery occurred within the metastable β phase, and with the increased deformation temperature, both the intragranular and grain boundary strengths declined, albeit with a sharper reduction in the grain boundary strength. At 650 °C, the weakest region in the polycrystalline alloys was the grain boundary. Consequently, the mechanism of grain boundary slip took precedence during elevated temperature deformation, with grain boundaries prone to microcrack formation due to their inherent weakness [17]. For the phase boundaries between Ti_5Si_3 and the matrix, however, it can be observed that in-situ precipitates displayed strong wettability and interfacial bonding. To summarize, the designed Ti alloy architecture optimized the synergistic properties at elevated temperatures via well-tailored phase constituents, interface characteristics, and dislocation mechanisms.

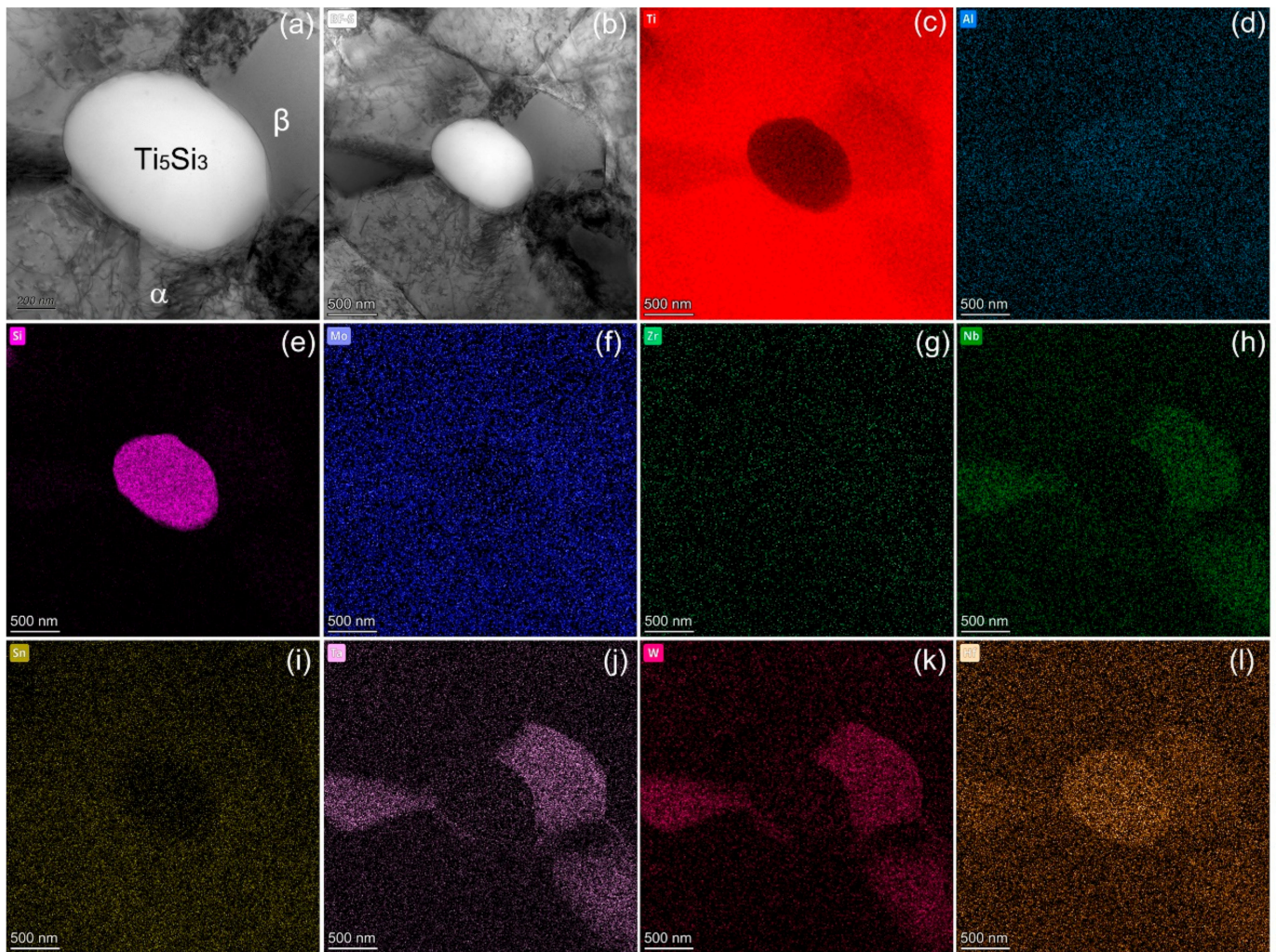


Figure 7. Typical bright field TEM images showing the microstructure after failure at 650 °C (a,b), as well as STEM elemental analysis (c–l).

4. Conclusions

In conclusion, this study presents a titanium alloy containing in-situ titanium silicide particles, for which the elevated temperature oxidation and tensile behaviors were thoroughly investigated and characterized. The main findings can be summarized as follows:

1. The alloy showed excellent resistance to oxidation at 600 °C and 700 °C. An oxidation reaction index (n) close to 2 and a small parabolic rate constant indicated favorable oxidation resistance. At 700 °C, the n value of 2.32 suggested that a diffusion mechanism governed the oxidation process, ensuring effective protection by the oxide film.
2. At 700 °C, the presence of oxidation-resistant Ti_5Si_3 particles at the phase boundaries hindered their full reaction with oxygen, acting as barriers to oxygen ingress. Conversely, at 800 °C, the oxidation was impacted by a strong interfacial reaction between oxygen and the oxide film/substrate. The resulting oxide film exhibited a porous structure with TiO_2 rods and irregular pores, indicating a dramatic decline in oxidation resistance at an elevated temperature.
3. The high temperature tensile data tested at 550 °C were $\sigma_y = 227.54$ MPa, $\sigma_t = 305.4$ MPa, $\epsilon = 107.7\%$; $\sigma_y = 113.52$ MPa, $\sigma_t = 142.58$ MPa, $\epsilon = 253.1\%$ at 600 °C; $\sigma_y = 42.41$ MPa, $\sigma_t = 54.11$ MPa, $\epsilon = 694.7\%$ at 650 °C. Notably, high deformations at 600 °C and 650 °C led to internal cracks in certain large Ti_5Si_3 particles; however, no interface debonding occurred due to the superior interface bonding strength with the matrix.

4. Microstructural analysis post-deformation indicated the presence of a complex dislocation structure, primarily within the α -Ti phase. The increased deformation temperatures led to decreased intragranular and grain boundary strengths, with the grain boundaries becoming the weakest points in the alloy at 650 °C. The grain boundaries were prone to microcrack formation during high-temperature deformation due to their inherent weakness. In contrast, the interfaces between the Ti_5Si_3 precipitates and the matrix exhibited robust interfacial bonding strength.

Author Contributions: Conceptualization, L.Z.; Methodology, K.J., W.H. and Y.Z.; Software, J.L., K.J., L.Z., B.C. and H.S.; Validation, B.C.; Formal analysis, J.L., K.J., L.Z. and H.S.; Investigation, K.J. and L.Z.; Resources, J.L. and B.C.; Data curation, L.Z.; Writing—original draft, L.Z.; Writing—review and editing, L.Z., B.C., H.S., W.H. and Y.Z.; Supervision, L.Z.; Project administration, L.Z.; Funding acquisition, L.Z. and B.C. All authors have read and agreed to the published version of the manuscript.

Funding: Financial support from Key Research and Development Projects of Shaanxi (No. 2021GY-214) and Jingying Innovative Talents Project of Xi'an Yingcai Plan (No. XAYC210048) are acknowledged.

Institutional Review Board Statement: Not applicable.

Informed Consent Statement: Not applicable.

Data Availability Statement: Data is contained within the article.

Conflicts of Interest: The authors confirm that they have no financial or personal affiliations with any individual or organization that might unduly bias their work. There are no professional or personal ties to any products, services, or companies that could be perceived as swaying the perspective or review of the manuscript in question.

References

1. Yang, Y.; Zhang, Y.; Liu, X.; Zhang, H. Study on cavitation corrosion properties of titanium alloy radiation rod with different roughnesses for ultrasonic casting. *Coatings* **2023**, *13*, 1632. [\[CrossRef\]](#)
2. Lu, W.J.; Zhuo, L.C. Additive manufacturing of titanium alloys via selective laser melting: Fabrication, microstructure, post-processing, performance and prospect. *Int. J. Refract. Met. Hard. Mater.* **2023**, *111*, 106110. [\[CrossRef\]](#)
3. Lin, Y.; Wang, H.; Zhang, M.; Lin, H.; Yan, D.; Lin, Q.; Kang, X.; Wang, X. Gradient coating of laser cladding TiB_2 /Ti-based alloy on titanium alloy surface. *Coatings* **2023**, *13*, 743. [\[CrossRef\]](#)
4. Graf, G.; Seyffertitz, M.; Spoerk-Erdely, P.; Clemens, H.; Stark, A.; Hatzenbichler, L. On the stability of $\text{Ti}(\text{Mn,Al})_2\text{C}_{14}$ Laves phase in an intermetallic Ti-42Al-5Mn alloy. *Intermetallics* **2023**, *161*, 107962. [\[CrossRef\]](#)
5. Pang, G.; Lin, Y.C.; Jiang, Y.; Zhang, X.; Liu, X.; Xiao, Y. Precipitation behaviors and orientation evolution mechanisms of α phases in Ti-55511 titanium alloy during heat treatment and subsequent hot deformation. *Mater. Charact.* **2020**, *167*, 110471. [\[CrossRef\]](#)
6. Dai, J.; Zhu, J.; Chen, C.; Weng, F. High temperature oxidation behavior and research status of modifications on improving high temperature oxidation resistance of titanium alloys and titanium aluminides: A review. *J. Alloys Compd.* **2016**, *685*, 784–898. [\[CrossRef\]](#)
7. Li, J.; Wang, L.; Qin, J.; Chen, Y.; Lu, W.; Zhang, D. Thermal stability of in situ synthesized $(\text{TiB}+\text{La}_2\text{O}_3)/\text{Ti}$ composite. *Mater. Sci. Eng. A* **2011**, *528*, 4883–4887. [\[CrossRef\]](#)
8. Li, J.; Wang, L.; Qin, J.; Chen, Y.; Lu, W.; Zhang, D. Effect of microstructure on high temperature properties of in situ synthesized $(\text{TiB}+\text{La}_2\text{O}_3)/\text{Ti}$ composite. *Mater. Charact.* **2012**, *66*, 93–98. [\[CrossRef\]](#)
9. Jiao, Y.; Huang, L.J.; Wei, S.L.; Geng, L.; Qian, M.F.; Yue, S. Nano- Ti_5Si_3 leading to enhancement of oxidation resistance. *Corros. Sci.* **2018**, *140*, 223–230. [\[CrossRef\]](#)
10. Yin, X.; Liang, J.; Gao, Y.; Lin, Z.; Chen, S.; Liu, C. Effects of LaB_6 on the high-temperature oxidation behavior of $\text{TiC} + \text{TiBx}$ reinforced titanium matrix composite coatings fabricated by laser cladding. *Surf. Coat. Technol.* **2021**, *421*, 127445. [\[CrossRef\]](#)
11. Xu, X.; Liu, Y.; Tabie, V.; Cai, C.; Xiao, Y.; Zhang, X. High-temperature oxidation resistance of a Ti-Al-Sn-Zr titanium matrix composites reinforced with in situ TiC and Ti_5Si_3 fabricated by powder metallurgy. *Appl. Phys. A* **2020**, *126*, 254. [\[CrossRef\]](#)
12. Xiong, Y.; Du, M.; Zhang, F.; Saba, F.; Shang, C. Preparation and mechanical properties of titanium alloy matrix composites reinforced by Ti_3AlC and TiC ceramic particulates. *J. Alloys Compd.* **2021**, *886*, 161216. [\[CrossRef\]](#)
13. Jiao, Y.; Huang, L.J.; Wang, S.; Li, X.T.; An, Q.; Cui, X.P. Effects of first-scale TiBw on secondary-scale Ti_5Si_3 characteristics and mechanical properties of in-situ $(\text{Ti}_5\text{Si}_3 + \text{TiBw})/\text{Ti6Al4V}$ composites. *J. Alloys Compd.* **2017**, *704*, 269–281. [\[CrossRef\]](#)
14. Hu, Z.; Cheng, X.; Li, S.; Zhang, H.; Wang, H.; Zhang, Z. Investigation on the microstructure, room and high temperature mechanical behaviors and strengthening mechanisms of the $(\text{TiB} + \text{TiC})/\text{TC4}$ composites. *J. Alloys Compd.* **2017**, *726*, 240–253. [\[CrossRef\]](#)
15. Qi, J.Q.; Chang, Y.; He, Y.Z.; Sui, Y.W.; Wei, F.X.; Meng, Q.K. Effect of Zr, Mo and TiC on microstructure and high-temperature tensile strength of cast titanium matrix composites. *Mater. Des.* **2016**, *99*, 421–426. [\[CrossRef\]](#)

16. Wang, H.W.; Qi, J.Q.; Zou, C.M.; Zhu, D.D.; Wei, Z.J. High-temperature tensile strengths of in situ synthesized TiC/Ti-alloy composites. *Mater. Sci. Eng. A* **2012**, *545*, 209–213. [[CrossRef](#)]
17. Yang, J.; Chen, Y.; Xiao, S.; Xu, L.; Wang, X.; Tian, J. High temperature tensile properties, deformation, and fracture behavior of a hybrid-reinforced titanium alloy composite. *Mater. Sci. Eng. A* **2020**, *788*, 139516. [[CrossRef](#)]
18. Zhao, Q.Y.; Yang, F.; Torrens, R.; Bolzoni, L. Evaluation of the hot workability and deformation mechanisms for a metastable beta titanium alloy prepared from powder. *Mater. Charact.* **2019**, *149*, 226–238. [[CrossRef](#)]
19. Pan, Y.; Li, W.; Lu, X.; Hayat, M.D.; Yin, L.; Song, W. Microstructure and tribological properties of titanium matrix composites reinforced with in situ synthesized TiC particles. *Mater. Charact.* **2020**, *170*, 110633. [[CrossRef](#)]
20. Akman, F.; Khattari, Z.Y.; Kaçal, M.R.; Sayyed, M.I.; Afaneh, F. The radiation shielding features for some silicide, boride and oxide types ceramics. *Radiat. Phys. Chem.* **2019**, *160*, 9–14. [[CrossRef](#)]
21. Jiao, Y.; Huang, L.J.; Wei, S.L.; Peng, H.X.; An, Q.; Jiang, S. Constructing two-scale network microstructure with nano-Ti₅Si₃ for superhigh creep resistance. *J. Mater. Sci. Technol.* **2019**, *35*, 1532–1542. [[CrossRef](#)]
22. Tang, Z.; Williams, J.J.; Thom, A.J.; Akinc, M. High temperature oxidation behavior of Ti₅Si₃-based intermetallics. *Intermetallics* **2008**, *16*, 1118–1124. [[CrossRef](#)]
23. Liu, C.; Huang, L.J.; Geng, L.; Jiao, Y.; Tang, A. In situ synthesis of (TiC + Ti₃SiC₂ + Ti₅Si₃)/Ti6Al4V composites with tailored two-scale architecture. *Adv. Eng. Mater.* **2015**, *17*, 933–941. [[CrossRef](#)]
24. Huang, K.; Han, X. High-temperature oxidation properties of Ti-Hf-Mo-Ta-Nb-B composite coating deposited on Ti60 alloy with laser cladding. *Coatings* **2023**, *13*, 1646. [[CrossRef](#)]
25. Lu, J.; Zhao, Y.; Du, Y.; Zhang, W.; Zhang, Y. Microstructure and mechanical properties of a novel titanium alloy with homogeneous (TiHf)₅Si₃ particle-reinforcements. *J. Alloys Compd.* **2019**, *778*, 115–123. [[CrossRef](#)]
26. Yang, Y.; Bewlay, B.P.; Chang, Y.A. Thermodynamic modeling of the Hf–Ti–Si ternary system. *Intermetallics* **2007**, *15*, 168–176. [[CrossRef](#)]
27. Xu, Y.; Fu, Y.; Li, J.; Xiao, W.; Zhao, X.; Ma, C. Effects of tungsten addition on the microstructural stability and properties of Ti-6.5Al-2Sn-4Hf-2Nb-based high temperature titanium alloys. *J. Mater. Sci. Technol.* **2021**, *93*, 147–156. [[CrossRef](#)]
28. Jiang, B.; Wen, D.; Wang, Q.; Che, J.; Dong, C.; Liaw, P.K. Design of near- α Ti alloys via a cluster formula approach and their high-temperature oxidation resistance. *J. Mater. Sci. Technol.* **2019**, *35*, 1008–1016. [[CrossRef](#)]
29. Guo, W.; Wang, H.; Peng, P.; Song, B.; Zhang, H.; Shao, T. Effect of laser shock processing on oxidation resistance of laser additive manufactured Ti6Al4V titanium alloy. *Corros. Sci.* **2020**, *170*, 108655. [[CrossRef](#)]
30. Dai, J.; Sun, C.; Wang, A.; Zhang, H.; Li, S.; Zhang, H. High temperature oxidation and hot corrosion behaviors of Ti2AlNb alloy at 923 K and 1023 K. *Corros. Sci.* **2021**, *184*, 109336. [[CrossRef](#)]
31. Bhattacharya, S.K.; Sahara, R.; Narushima, T. Predicting the parabolic rate constants of high-temperature oxidation of Ti alloys using machine learning. *Oxid. Met.* **2020**, *94*, 205–218. [[CrossRef](#)]
32. Lim, H.P.; Liew, W.Y.; Melvin, G.J.; Jiang, Z. A short review on the phase structures, oxidation kinetics, and mechanical properties of complex Ti–Al alloys. *Materials* **2021**, *14*, 1677. [[CrossRef](#)] [[PubMed](#)]
33. Chen, C.; Chen, M.; Xie, L.; Gong, Z.; Ye, J. Numerical and experimental investigations of the hot stamping process for complex aircraft skin parts composed of TA32 high-temperature titanium alloy using an Arrhenius-type constitutive model. *Int. J. Adv. Manufact. Technol.* **2019**, *103*, 807–817. [[CrossRef](#)]
34. Li, H.; Ding, Q.; Gu, Y.; Li, G.; Zhang, Y.; Zhang, Y. The initial oxidation behavior of uranium and uranium-titanium alloys in standing storage. *Corros. Sci.* **2020**, *176*, 108879. [[CrossRef](#)]
35. Vaché, N.; Cadoret, Y.; Dod, B.; Monceau, D. Modeling the oxidation kinetics of titanium alloys: Review, method and application to Ti-64 and Ti-6242s alloys. *Corros. Sci.* **2021**, *178*, 109041. [[CrossRef](#)]
36. Wang, T.; Wang, L.; Lu, Q.; Fan, Z. Changes in the esthetic, physical, and biological properties of a titanium alloy abutment treated by anodic oxidation. *J. Prosthet. Dent.* **2019**, *121*, 156–165. [[CrossRef](#)] [[PubMed](#)]
37. Wu, B.; Xiong, S.; Guo, Y.; Chen, Y.; Huang, P.; Yang, B. Tooth-colored bioactive titanium alloy prepared with anodic oxidation method for dental implant application. *Mater. Lett.* **2019**, *248*, 134–137. [[CrossRef](#)]
38. Bi, X.; Du, G.; Kalam, A.; Sun, D.; Yu, Y.; Su, Q. Tuning oxygen vacancy content in TiO₂ nanoparticles to enhance the photocatalytic performance. *Chem. Eng. Sci.* **2021**, *234*, 116440. [[CrossRef](#)]
39. Dwivedi, C.; Mohammad, T.; Kumar, V.; Dutta, V. Ti³⁺ and oxygen defects controlled colored TiO₂ nanoparticles by continuous spray pyrolysis. *Vacuum* **2020**, *182*, 109612. [[CrossRef](#)]
40. Chong, Y.; Poschmann, M.; Zhang, R.; Zhao, S.; Hooshmand, M.S.; Rothchild, E. Mechanistic basis of oxygen sensitivity in titanium. *Sci. Adv.* **2020**, *6*, e4060. [[CrossRef](#)]
41. Li, C.; Huang, L.; Zhao, M.; Guo, S.; Li, J. Hot deformation behavior and mechanism of a new metastable β titanium alloy Ti-6Cr-5Mo-5V-4Al in single phase region. *Mater. Sci. Eng. A* **2021**, *814*, 141231. [[CrossRef](#)]
42. Lei, J.; Zhu, W.; Chen, L.; Sun, Q.; Xiao, L.; Sun, J. Deformation behavior and microstructural evolution during the hot compression of Ti-5Al4Zr8Mo7V alloy. *Mater. Today Commun.* **2020**, *23*, 100873. [[CrossRef](#)]
43. Ling, K.; Mo, W.; Deng, P.; Chen, J.; Luo, B.; Bai, Z. Hot deformation behavior and dynamic softening mechanisms of hot-extruded Al-Cu-Mg-Ag-Mn-Zr-Ti alloy. *Mater. Today Commun.* **2023**, *34*, 105300. [[CrossRef](#)]
44. Ji, X.; Guo, B.; Jiang, F.; Yu, H.; Fu, D.; Teng, J. Accelerated flow softening and dynamic transformation of Ti-6Al-4V alloy in two-phase region during hot deformation via coarsening α grain. *J. Mater. Sci. Technol.* **2020**, *36*, 160–166. [[CrossRef](#)]

45. Guo, B.; Semiatin, S.L.; Jonas, J.J. Dynamic transformation during the high temperature deformation of two-phase titanium alloys. *Mater. Sci. Eng. A* **2019**, *761*, 138047. [[CrossRef](#)]
46. Roy, S.; Suwas, S. Orientation dependent spheroidization response and macro-zone formation during sub β -transus processing of Ti-6Al-4V alloy. *Acta Mater.* **2017**, *134*, 283–301. [[CrossRef](#)]
47. Agrawal, P.; Karthikeyan, S.; Makineni, S.K.; Gault, B.; Banerjee, D. Dynamic strain aging in the intermediate temperature regime of near- α titanium alloy, IMI 834: Experimental and modeling. *Acta Mater.* **2022**, *222*, 117436. [[CrossRef](#)]
48. Prasad, K.; Sarkar, R.; Ghosal, P.; Varma, V.K. The influence of dynamic strain aging on the low cycle fatigue behavior of near alpha titanium alloy IMI 834. *Mater. Sci. Eng. A* **2008**, *494*, 227–231. [[CrossRef](#)]
49. Chang, X.; Qi, Y.; Chen, X.; Xie, Z.; Zhang, P.; Chen, G. Extra work hardening and activation of softening mechanisms induced by α - β interactions of a metastable- β Ti alloy during sub-transus processing. *Mater. Sci. Eng. A* **2023**, *865*, 144653. [[CrossRef](#)]
50. Joseph, S.; Bantounas, I.; Lindley, T.C.; Dye, D. Slip transfer and deformation structures resulting from the low cycle fatigue of near-alpha titanium alloy Ti-6242Si. *Int. J. Plast.* **2018**, *100*, 90–103. [[CrossRef](#)]
51. Wang, T.; Guo, H.; Wang, Y.; Peng, X.; Zhao, Y.; Yao, Z. The effect of microstructure on tensile properties, deformation mechanisms and fracture models of TG6 high temperature titanium alloy. *Mater. Sci. Eng. A* **2011**, *528*, 2370–2379. [[CrossRef](#)]
52. Wei, S.; Zhu, G.; Tasan, C.C. Slip-twinning interdependent activation across phase boundaries: An in-situ investigation of a Ti-Al-V-Fe ($\alpha + \beta$) alloy. *Acta Mater.* **2021**, *206*, 116520. [[CrossRef](#)]

Disclaimer/Publisher’s Note: The statements, opinions and data contained in all publications are solely those of the individual author(s) and contributor(s) and not of MDPI and/or the editor(s). MDPI and/or the editor(s) disclaim responsibility for any injury to people or property resulting from any ideas, methods, instructions or products referred to in the content.